



Boosting electrochemical CO₂ reduction to CO over interfacial hydroxide-metal catalysts

Liang Fu, Zhenping Qu ^{*}, Lingling Zhou, Yue Ding

Key Laboratory of Industrial Ecology and Environmental Engineering (Ministry of Education, China), School of Environmental Science and Technology, Dalian University of Technology, Linggong Road 2, Dalian 116024, China



ARTICLE INFO

Keywords:
Electrochemical CO₂ reduction
Silver
Indium hydroxide
Interface
In situ Raman spectroscopy

ABSTRACT

Interface engineering is demonstrated to lead to significant improvement in the catalytic performance for electrochemical CO₂ reduction reactions (CO₂RR). In this work, we demonstrate a heterogeneous In(OH)₃-Ag interface catalyst in which the appropriate In(OH)₃ clusters modified on metal Ag nanoparticles surface greatly improves the CO selectivity in CO₂RR, realizing a CO faradaic efficiency (FE_{CO}) of 93% at -0.7 V vs. RHE. The performance enhancement is attributed to the preferentially CO₂ adsorption and activation by the In(OH)₃-Ag interface sites. *In situ* Raman spectroscopy reveals that the formation of In(OH)₃-Ag interface sites is significantly favorable for the generation of key $^{*}\text{CO}_2$ intermediate at low overpotential. Further theoretical calculation confirms that the In(OH)₃-Ag interface could enhance the adsorption of $^{*}\text{COOH}$ species on catalyst by means of tailoring the surface properties and electronic structures. This work shows that hydroxide-metal interface engineering is a promising pathway to regulate the activity for selective CO₂RR properties.

1. Introduction

Electrochemical CO₂ reduction reaction (CO₂RR) is considered one of the most promising carbon capture and utilization (CCU) because CO₂RR can convert CO₂ into fuels or chemical raw materials, showing potential application prospects that have strategic importance for industrial development and the feasible anthropogenic chemical recycling of CO₂ [1-3].

The main challenge of CO₂RR is the design of catalyst with high performance to reduce the overpotential and improve the product selectivity [4]. Various materials have been employed as electrocatalysts to convert CO₂ via CO₂RR [5-8]. Interface engineering has been proved to be an effective strategy to break the scaling relationship and change the adsorption characteristics of reactant molecules at the interface to obtain high performance catalysts, but the selection and design principles of materials in interface engineering need to be further in-depth investigation [9-11]. Bao et al. first pioneered the research on the Au-CeO_x interface for CO₂RR to CO [12]. Au-CeO_x interface showed a CO geometric current density 1.6 times than that of Au/C at -0.89 V vs. RHE, which led to a CO Faradaic efficiency of 89.1%. However, the overpotential was high for CO₂ conversion. Density functional theory calculations indicated that the Au-CeO_x interface was the active site for

CO₂ activation and the reduction to CO, and the synergy between Au and CeO_x in the Au-CeO_x composite promoted the stability of the-COOH intermediate. At the same time, it was impressive that Bao et al. pointed out that hydroxyl groups from water dissociation could further enhance the reduction of CeO_x and the stability of CO₂^Δ species. Sargent et al. proved that the hydroxide had stronger water dissociation ability than oxide, and changed the adsorption energy of hydrogen on surface loaded copper, which affected the protonation process of reaction intermediates, and finally changed the selectivity of product from ethylene to ethanol [13]. Perez-Ramirez et al. deposited Ag nanoparticles onto In(OH)₃ and In₂O₃ supports, respectively, and studied the metal-support interaction in detail [14]. Unfortunately, In₂O₃ was reduced to metal In within the first 40 min of electrolysis, leading to the *in situ* formation of Ag and In mixed phase and a rapid decrease in current density (at around one-tenth of the initial value). Compared with In₂O₃, the reduction resistance of In(OH)₃ support was better under CO₂RR conditions, and the synergistic effect of Ag and In(OH)₃ was more favorable to improve the CO selectivity (CO faradaic efficiency over 40Ag/IH was $\sim 65\%$ at -0.6 V vs. RHE while pure Ag had a faradaic efficiency of $\sim 30\%$ at same potential). However, this CO selective enhancement mechanism was not well understood, and this level of CO selectivity was still not ideal due to the exposure of large amounts of In(OH)₃ for the formation

* Corresponding author.

E-mail address: quzhenping@dlut.edu.cn (Z. Qu).

of formic acid.

In conclusion, hydroxides may be a better choice than oxides in the field of CO₂RR because of their sufficient resistance to reduction and greater ability to water dissociation [15]. Herein, the In(OH)₃-Ag interface was constructed by decorating In(OH)₃ clusters on the surface of Ag nanoparticles. We evaluated the effect of the amount of decoration of In(OH)₃ on the CO selectivity, emphasizing the importance of interface interaction for enhancing CO₂RR performance. Compared to Ag/C and In(OH)₃/C, the optimized In(OH)₃-Ag/C displayed a better catalytic selectivity in the electrochemical reduction of CO₂ into CO, realizing the FE_{CO} of 93% at -0.7 V vs. RHE. *In situ* Raman spectroscopy had also been used to monitor the changes of intermediate states for CO₂RR. The corresponding density functional theory (DFT) calculation also examined the effect of In(OH)₃ decoration. These findings may help to understand the role of hydroxides in interfacial enhancement of CO₂RR performance.

2. Experimental

2.1. Chemicals and materials

Silver nitrate (AgNO₃, 99.8%), sodium citrate (C₆H₅Na₃O₇·2 H₂O, 99.0%), sodium borohydride (NaBH₄, 98%) and potassium bicarbonate (KHCO₃, 99.5%) were purchased from Sinopharm Chemical Reagent Co., Ltd. Indium nitrate (In(NO₃)₃·xH₂O, 99.9%) was purchased from Shanghai Aladdin Biochemical Technology Co., Ltd. Ethanol (C₂H₅OH, 99.7%) was purchased from Tianjin Fuyu Fine Chemical Co., Ltd. Polytetrafluoroethylene (PTFE, 60 wt% dispersion in H₂O) were purchased from Sigma-Aldrich. Nafion 117 ionomer (~5 wt% in a mixture of lower aliphatic alcohols and water) was purchased from Macklin. Nafion 117 proton exchange membrane was purchased from Dupont. Toray TGP-H-060 carbon paper and Vulcan XC-72R carbon black (CB) were purchased from Toray Industries and Cabot Corporation, respectively. Ultrapure deionized water (18.2 MΩ) was used throughout this work. All the chemicals were used without further purification.

2.2. Catalysts synthesis

The In(OH)₃-Ag/C catalyst was prepared by liquid phase reduction method [12,16]. The detailed synthesis procedure for In(OH)₃-Ag/C catalyst (the atomic ratio of Ag/In was set at 95/5) was as follow: 89.8 mg AgNO₃, 7.86 mg In(NO₃)₃·xH₂O and 1270.5 mg sodium citrate were dissolved in 200 mL deionized water, which was then sonicated for 30 min until the solution was uniform. Afterwards, 240 mg XC-72R carbon black was added into the above solution and dispersing in the ultrasonic instrument for 60 min. Transfer the disperse solution to the ice bath, stir vigorously, then a new configuration of 50 mL 0.1 M of NaBH₄ solution was added dropwise, followed by stirring at 300 rpm for 12 h. Finally, the product was washed with 500 mL deionized water, and drying at 60 °C for 12 h under vacuum. In particular, only AgNO₃ and In (NO₃)₃·xH₂O was added for Ag/C and In(OH)₃/C catalyst synthesis, respectively. In₂O₃-Ag/C was obtained by calcining In(OH)₃-Ag/C in an Ar atmosphere at 400 °C for 1 h in tubular furnace. Other catalysts with various Ag/In feeding ratios (e.g., 98/2, 90/10, and 80/20) were also prepared via the same approach as a contrast.

2.3. Physicochemical characterizations

X-ray diffraction (XRD) patterns were collected by the Rigaku D/MAX-2500/PC diffractometer with Cu K_α as the X-ray source ($\lambda = 1.5418$ Å). The tube voltage was 40 kV and tube current was 100 mA. XRD data were recorded at room temperature from 20° to 80° for 20 Bragg angle at a scanning rate of 5° min⁻¹. Fourier transforms infrared (FT-IR) spectra were collected at Bruker Vertex 70 infrared spectrometer at a resolution ratio of 4 cm⁻¹ in the wavenumber range of 4000–500 cm⁻¹ with scanning for 32 times at room temperature by using the KBr

pressed-disk technique. UV-visible (UV-vis) diffuse reflectance spectra were acquired with Shimadzu UV-2600. Barium sulfate powder was used as a reference, and the scanning range was 190–800 nm. Transmission electron microscopy (TEM) measurements were carried out by JEM-2100 microscope. The acceleration voltage was 200 kV and the beam intensity was 200 nA (15 kV). High resolution transmission electron microscopy (HRTEM) images were acquired from the JEM-ARM200F electron microscope equipped with high angle annular dark-field (HAADF) and energy dispersive X-ray spectroscopy (EDS) detectors operated at 200 kV and measured the information resolution better than 0.12 nm. X-ray photoelectron spectroscopy (XPS) spectra were obtained from a Thermo Fisher Scientific ESCALAB 250Xi spectrometer and the excitation source was Al K_α. Behind purging the samples, the spectra were recorded at ambient temperature under vacuum conditions (residual pressure $< 10^{-7}$ Pa). All the XPS peaks were corrected by C 1 s (284.0 eV) peak. Gauss/Lorentz line shape fitting was used for all the peaks in the background of the Shirley algorithm. CO₂ Temperature programmed desorption (CO₂-TPD) experiments were carried out on a quadrupole mass spectrometer (QMS, Pfeiffer OmniStar 320) equipped with a computer-interfaced as the detector. Prior to each experiment, fresh catalyst (100 mg) went through the pre-treatment amidst the He atmosphere at 150 °C for 30 min to clean the sample surface. Upon coming down to room temperature, the samples were saturated with pure CO₂ at room temperature for 60 min, followed by introducing He to get rid of the weakly physical absorption molecule. Subsequently, the TPD experiment was conducted in flowing He with a rising rate of 10 °C min⁻¹, and the desorbed CO₂ data was acquired by the mass spectrometer.

2.4. Electrochemical measurements

All the electrochemical experiments were carried out in a gas-tight H-type electrolysis cell using an electrochemical workstation (CHI 660E). The two chambers were separated by a Nafion 117 proton exchange membrane, where Ag/AgCl and Pt wire were used as reference electrode (RE) and counter electrode (CE), respectively. The working electrode was prepared by immobilization of the electrocatalyst on carbon paper (2.1 cm × 2.1 cm) equipped with the gas diffusion layer (GDL). Typically, the as-prepared catalyst with a mass ratio of 9:1 with Nafion solution was ultrasonically dispersed in ethanol to form a uniform ink. The formed ink was evenly brushed onto carbon paper and the catalyst loading in GDL was 2.0 ± 0.1 mg cm⁻². The 0.1 M KHCO₃ electrolyte was saturated by bubbling CO₂ gas (99.999%) for 30 min at a flow rate of 20 mL min⁻¹ before the electrochemical measurement and continuously fed during the test. The pH of the CO₂-saturated 0.1 M KHCO₃ electrolyte was 6.8. The measured potential of CO₂RR was compared with a reversible hydrogen electrode (RHE) using the following equation: $E_{(vs. RHE)} = E_{(vs. Ag/AgCl)} + 0.197 V + 0.0591 \times pH$.

Linear sweep voltammetry (LSV) curve was carried out in Ar-saturated and CO₂-saturated 0.1 M KHCO₃ electrolyte at a scan rate of 10 mV s⁻¹. Electrochemical impedance spectroscopy (EIS) was recorded at -0.5 V vs. Ag/AgCl in the frequency range of 10⁵ Hz to 10 Hz under CO₂-saturated atmospheres. Electrochemical active surface area (ECSA) was compared by electrochemical double-layer capacitance (C_{dl}) of the catalytic surface, where cyclic voltammetry (CV) curves were recorded in CO₂-saturated 0.1 M KHCO₃ electrolyte. The potential window was chosen in which no obvious faradaic reactions occurred. The geometrical current densities versus the scan rate of CV curves were plotted for each electrode and the C_{dl} was estimated from the slope of the linear regression.

2.5. Products analysis

Gas products were analyzed using a gas chromatograph (GC7900) outfitted with a flame ionization detector (FID) and a thermal conductivity detector (TCD), and the sample loop connected to the outlet of the

electrolysis cell. The liquid products were quantified by analyzing the electrolyte after the experiment using an ion chromatograph (CIC-D100). All the products on each electrode were repeatedly sampled and analyzed at least three times. The faradaic efficiency (FE) of gas and liquid products were acquired through their concentration and calculated by the following equation, $FE_{\text{gas}} = (z \cdot P \cdot F \cdot V \cdot v_i) / (R \cdot T \cdot J)$ and $FE_{\text{liquid}} = (z \cdot c \cdot V_0 \cdot F) / (J \cdot t)$, where z is the number of electrons transferred per mole of gas (CO and H₂ are both 2), P is the standard atmospheric pressure of 1.01×10^5 Pa, F is The Faraday constant of 96485 C mol⁻¹, V is the flow rate of cathode gas in the electrolytic cell of 3.33×10^{-7} m³ s⁻¹, v_i is the volume concentration of cathode single gas product, R is the ideal gas constant 8.314 J mol⁻¹ K⁻¹, T is 298.15 K at room temperature, J is the steady-state current (A) at each applied potential, c is the concentration of methyl acid in cathode electrolyte (mol L⁻¹), V_0 is the volume of cathode electrolyte (L), and T is the reaction time (s) of CO₂RR.

2.6. In situ Raman measurements

Raman spectral signals were collected by Renishaw (InVia Reflex) confocal laser Raman spectrometer equipped with 532 nm (the power was about 5 mW) wave-length laser and the data was collected by corresponding software (Wire) in the Raman shift from 200 to 2200 cm⁻¹. A 50 \times long working distance objective and a 90° adaptor were used. The Raman shift was calibrated to 520 cm⁻¹ using a Si wafer. Each Raman spectrum displayed here was recorded with 15 accumulations over an acquisition time of \sim 30 s. The H-type *in situ* Raman electrolysis cell (GaossUnion, China) consisted of three electrodes including RE (Ag/AgCl), CE (Pt wire) and WE (Ag/C or In(OH)₃-Ag/C). The electrolyte was CO₂-saturated 0.1 M KHCO₃ with a 0.5 mL min⁻¹ flow rate, and CO₂ was continuously bubbled into the electrolyte at a rate of 20 mL min⁻¹.

2.7. DFT calculations

All the periodic calculation was performed by the Quickstep module in CP2K [17]. The spin-polarized Perdew-Burke-Ernzerhof (PBE) exchange-correlation functional combined with molecularly optimized double-zeta valence plus polarization (DZVP) basis set was adopted for electronic structure calculation [18,19]. A 400 Ry energy was used for the Gaussian and Plane wave (GPW) scheme of plane wave (PW) cutoff. Core electrons were modeled by Geodecker-Teter-Hutter (GTH) pseudo potentials with 11, 13, 6, 1, 4 valence electrons for Ag, In, O, H, C, respectively [20,21]. Wavefunction analysis was calculated by Multiwfns package, and all images were rendered by VESTA program [22,23].

Ag(111) -p(4 \times 7)R60° surface slab was used to model the Ag substrate. The slab model consisted of four Ag atom layers. All models were optimized to be fully relaxed without any constraint. A 15 angstrom vacuum layer was combined with Martyna-Tuckerman (MT) correction to avoid the pteriodic images interaction in surface normal [24]. Four In(OH)₃ clusters were chosen to model small sub-nanometer-sized Indium oxide. In this work, the adsorption energy (E_{ads}) was calculated by

following equation:

$$E_{\text{ads}} = E_{\text{(total)}} - E_{\text{(mol)}} - E_{\text{(slab)}}$$

Where $E_{\text{(total)}}$ is the total energy of molecule adsorbed on slab, $E_{\text{(mol)}}$ is the energy of an isolated molecule, and $E_{\text{(slab)}}$ is the energy of clean slab.

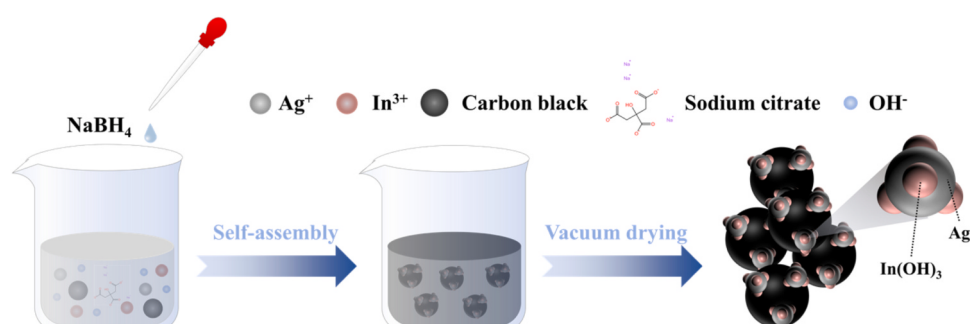
3. Results and discussion

3.1. Synthesis and characterization

As illustrated in Scheme 1, Carbon-supported In(OH)₃-Ag composite catalysts (In(OH)₃-Ag/C) with a total metal loading of 20 wt% was prepared with sodium citrate as the complexing agent and NaBH₄ as the reducing agent and the atomic ratio of Ag/In was set at 95/5 (the details synthesis method are provided in the Experimental section). In the process of catalyst self-assembly, Ag⁺ was rapidly reduced to Ag nanoparticles due to its high redox potential. On the other hand, since the hydrolysis rate of NaBH₄ was faster than that of In³⁺, In³⁺ will eventually form In(OH)₃ and deposit on the surface of Ag nanoparticles to form the In(OH)₃-Ag heterostructure. Ag/C and In(OH)₃/C catalysts were also prepared as the reference in the same way. In addition, more control samples of In(OH)₃-Ag composite catalysts with various Ag/In feeding ratios (e.g., 98/2, 90/10, and 80/20) were also prepared *via* the same approach.

Low magnification TEM images showed that Ag/C catalyst existed in the form of nanoparticles with an average size of \sim 18.8 nm on the surface of carbon support (Fig. S1), and In(OH)₃/C catalyst had no clear geometrical morphology with the form of accumulation (Fig. S2). The powder X-ray diffraction (XRD) confirmed the crystalline nature of Ag phase (JCPDS No. 04-0783) and In(OH)₃ phase (JCPDS No. 76-1463), respectively (Fig. 1a) [25]. The broad peak close to 25° was attributed to the carbon supports in these catalysts. For In(OH)₃-Ag/C catalyst (Ag/In = 95/5), the structure of Ag nanoparticles remained unchanged after the deposition of In(OH)₃, but the nanoparticles dimension showed a rather narrow size range of about \sim 8.1 nm compared with Ag/C catalyst (Fig. S3), which could be attributed that the introduced In³⁺ provided the dissimilar boundaries in the process of Ag nanoparticles growth, leading to the decrease of the grain size for Ag nanoparticles [26]. In(OH)₃-Ag/C catalyst only gave a clear crystalline response for Ag phase (Fig. 1a), excluding the formation of specific alloys or intermetallic compounds [27]. And there was no obvious diffraction peak related to In(OH)₃ phase, which could be attributed to the small size of the nanocrystals and/or the amorphous structure [28,29]. More In(OH)₃-Ag/C samples with various Ag/In ratios (98/2, 90/10, and 80/20) also showed the similar structure and morphology to that of Ag/In = 95/5 and a rather narrow size range compared with Ag/C catalyst (Fig. S4-S7, Table S1).

Fourier transforms infrared (FT-IR) spectra (Fig. 1b) presented that In(OH)₃-Ag/C catalyst showed the same characteristic absorption peaks of natural In(OH)₃ at 850 cm⁻¹ (O-H bending vibration), 1161 cm⁻¹,



Scheme 1. Schematic illustration for the synthesis of In(OH)₃-Ag/C catalyst.

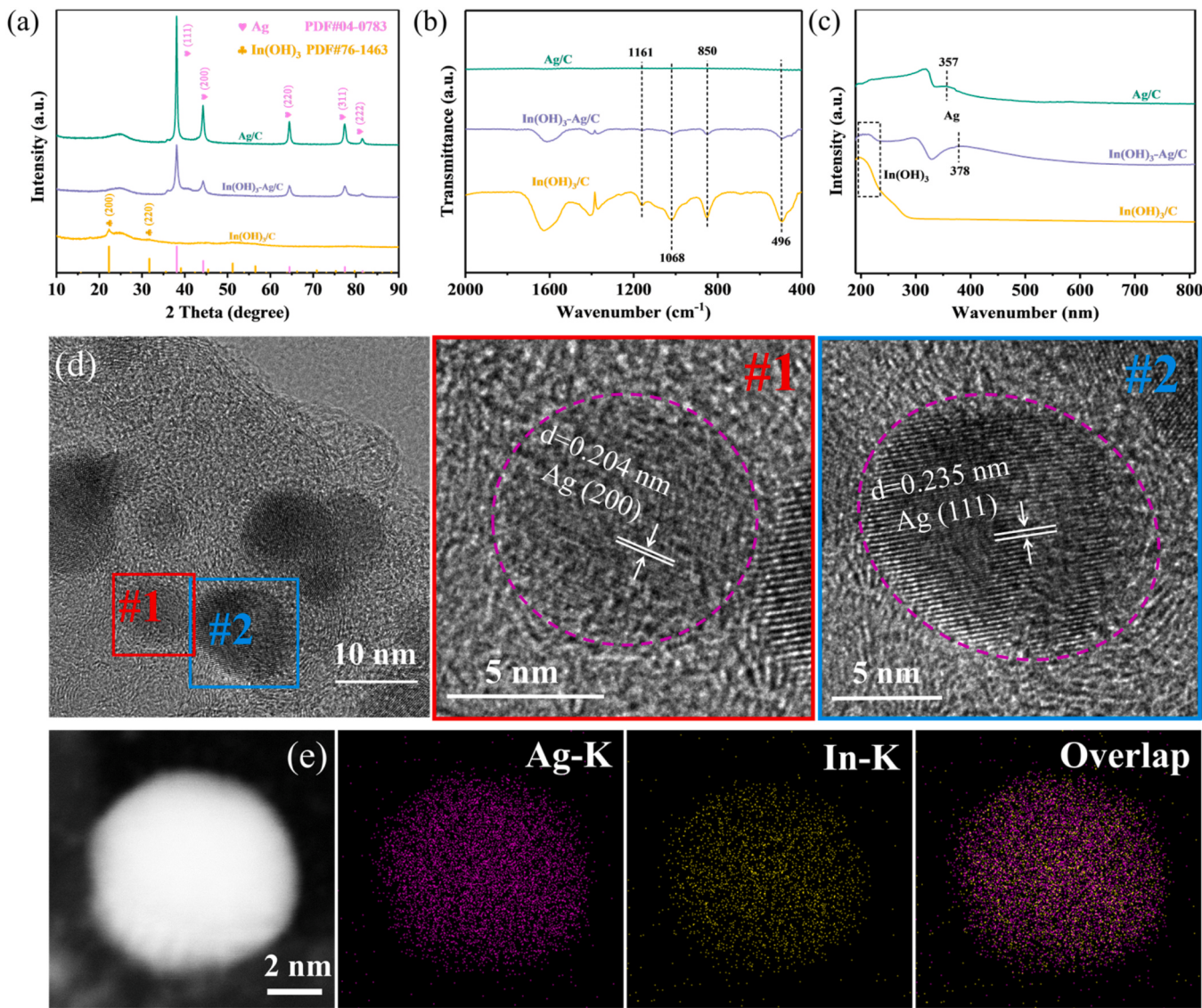


Fig. 1. (a) XRD patterns, (b) FT-IR spectra and (c) UV-vis diffuse reflectance spectra of Ag/C, In(OH)₃-Ag/C and In(OH)₃/C catalyst. (d) HRTEM images of In(OH)₃-Ag/C. (e) HAADF-STEM image and the corresponding EDS elemental mapping of In(OH)₃-Ag/C.

1068 cm⁻¹ and 496 cm⁻¹ (In-OH absorption bands), indicating the presence of In(OH)₃ in the synthetic sample [26,30]. Other samples with various Ag/In feeding ratios (98/2, 90/10, and 80/20) showed the similar peak locations compared to In(OH)₃-Ag/C catalyst (Fig. S8). Upon In(OH)₃ attachment, the surface plasmon resonance peak of the Ag nanoparticles moved from 357 to 378 nm, as recorded in the ultraviolet-visible (UV-vis) absorption spectra (Fig. 1c). This red shift can be attributed to the quantum size effect by the decrease of the grain size of Ag [31]. However, the corresponding peak position for Ag/In=80/20 with more In(OH)₃ contents exhibited the further red shift (Fig. S9), despite a slight increase in particle size compared to Ag/In = 95/5 (Fig. S3 and S6). This may be associated with a higher content of In(OH)₃ that caused a change in the surface refractive index [32]. In addition, the significant peak of In(OH)₃ owing to the interband transition of electrons (<235 nm) was observed, confirming the existence of In(OH)₃ [26].

A typical Ag (111) and Ag (200) plane was observed by the high-resolution transmission electron microscopy (HRTEM) with a characteristic lattice spacing of 0.235 nm and 0.204 nm on In(OH)₃-Ag/C catalyst, respectively (Fig. 1d), which was consistent with the results measured by XRD. Noteworthily, it was difficult to distinguish In species

here due to its amorphous form and/or high dispersion. Therefore, the high-angle annular dark field-scanning transmission electron microscopy (HAADF-STEM) and the energy-dispersive X-ray spectroscopy (EDS) elemental mapping were conducted (Fig. 1e). And It was observed that In species was indeed highly dispersed on the Ag surface and free of aggregation, which agreed well with the similar nanomaterials synthesized at low temperature [33]. Obviously, these results indicated the successful preparation of the heterogeneous In(OH)₃-Ag interface.

In order to further confirm the interface interaction of In(OH)₃-Ag/C catalyst, the chemical states of Ag and In were studied by X-ray photo-electron spectroscopy (XPS) measurement (Fig. 2a,b) and the quantitative results were summarized in Table S1. Notably, In(OH)₃-Ag/C catalyst showed a higher surface In amount (10.6%) detected by XPS than the feeding ratio (Ag/In = 95/5), which was consistent with the HRTEM results that In(OH)₃ were all located on the Ag nanoparticles surface. The binding energies of Ag 3d and In 3d electrons were recorded at 368.6/374.6 and 445.5/453.1 eV for Ag/C and In(OH)₃/C, characteristic of metal Ag⁰ and ionic In³⁺ states, respectively [34–36]. For In(OH)₃-Ag/C catalyst, both the Ag 3d and In 3d binding energy shift to the lower values compared to Ag/C and In(OH)₃/C, indicating an increase in the oxidation state of Ag and a decrease for that of In. With the

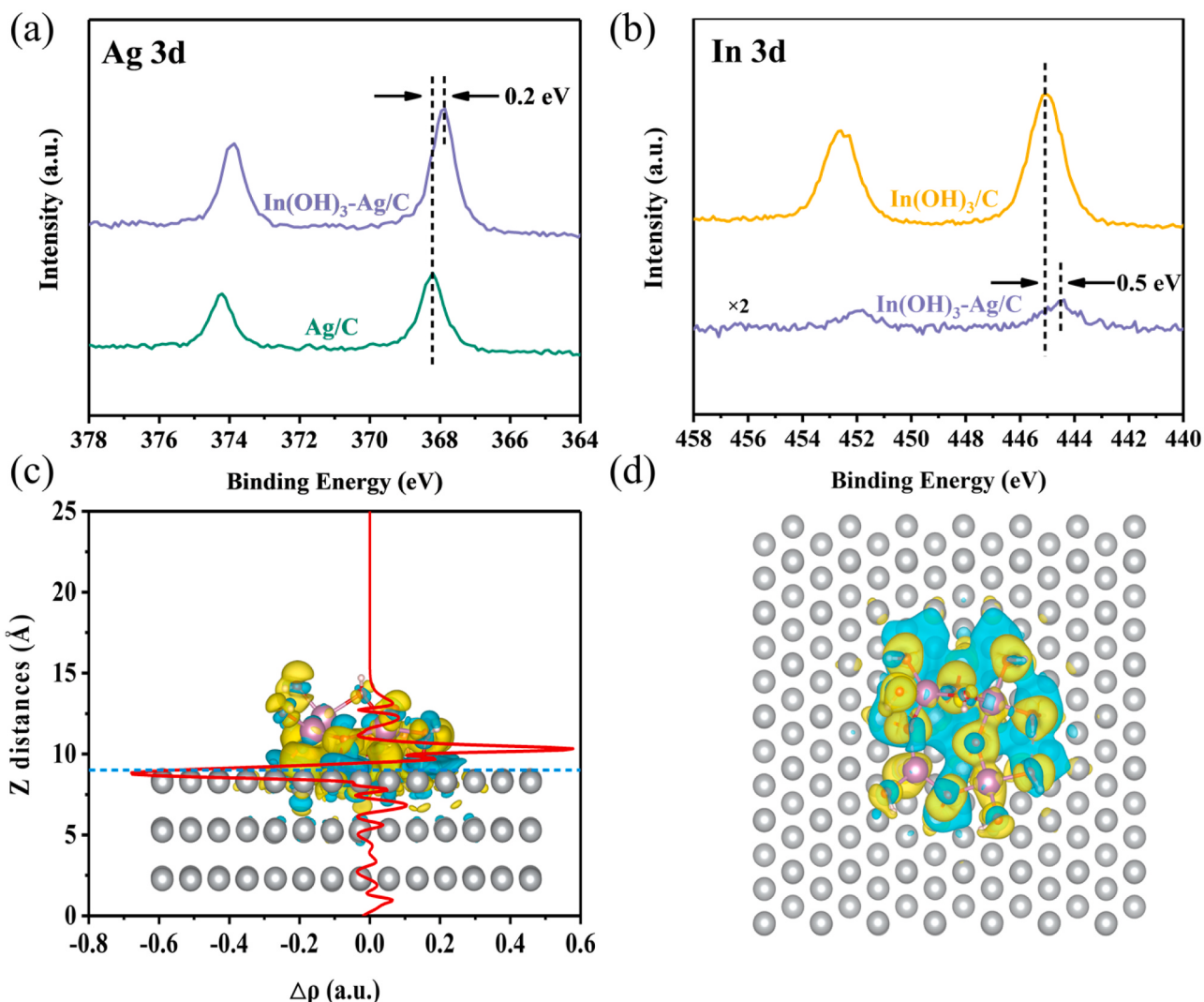


Fig. 2. (a) Ag 3d XPS spectra of Ag/C and In(OH)₃-Ag/C. (b) In 3d XPS spectra of In(OH)₃/C and In(OH)₃-Ag/C. (c) In(OH)₃/Ag(111) charge density difference. (d) Local integral curve of electron density difference along the Z direction. The yellow and cyan isosurface are 0.013 and -0.013 a.u., representing the increase and decrease of electron density respectively. Grey balls are Ag, purple balls are In, and red balls are O.

increase of In(OH)₃ amount, the Ag peak gradually shift to lower binding energy. Correspondingly, the In 3d peak displayed a shift to higher binding energy with its content increasing (Fig. S10). This result confirmed the formation of the In(OH)₃-Ag interface and the modified electronic structures between them [37]. This variation in XPS can also be explained by In(OH)₃/Ag(111) charge density difference results and four In(OH)₃ clusters on the Ag(111) surface was constructed to model the In(OH)₃-Ag interface (Fig. 2c,d). As depicted, the electron delocalization occurs at the Ag side of the In(OH)₃-Ag interface, and the electron will be transferred to the In(OH)₃ side of the In(OH)₃-Ag interface, which led to the decrease of the valence of interface Ag species. This finding is in good consistency with the experimental XPS results.

3.2. Electrochemical performance

The electrocatalytic properties of the prepared catalysts were initially investigated by linear sweep voltammetry (LSV) measurements in Ar- and CO₂-saturated 0.1 M KHCO₃ electrolyte (Fig. 3a). The as-prepared catalysts were loaded onto carbon paper to serve as a working electrode. Obviously, all electrodes showed the higher current densities in CO₂ conditions than those in Ar conditions, demonstrating the active nature of these electrodes in reducing CO₂ rather than H₂O [38]. More importantly, In(OH)₃-Ag/C catalyst exhibited much higher

current density than that of Ag/C and In(OH)₃/C catalyst under CO₂ conditions, indicating that In(OH)₃-Ag/C catalyst probably had higher electrocatalytic properties. Two cathodic peaks at about -0.7 V and -0.9 V vs. Ag/AgCl can be observed on the LSV curve of the In(OH)₃-Ag/C electrode in CO₂-saturated 0.1 M KHCO₃ electrolyte, which correspond to the reduction of oxidized states of Ag and indium oxide/hydroxide on the electrode surface respectively [39–41]. It is worth noting that the reduction peak at about -0.9 V vs. Ag/AgCl on the In(OH)₃-Ag/C electrode in CO₂-saturated 0.1 M KHCO₃ electrolyte is significantly larger than that in Ar-saturated 0.1 M KHCO₃ electrolyte, suggesting that the reduction peak may also be influenced by CO or other adsorption species [29,40].

The CO₂RR performance of In(OH)₃-Ag/C catalyst was investigated by using a three-electrode gas-tight H-type electrolysis cell with CO₂-saturated 0.1 M KHCO₃ electrolyte and compared with Ag/C and In(OH)₃/C. Ag/C catalyst was able to reduce CO₂ to CO in the more negative potential range, with the highest Faradaic efficiency (FE) of 65% at -0.9 V vs. RHE, and H₂ was the other dominant product in the entire potential range studied (Fig. S11). In(OH)₃/C was also active for CO₂RR, with HCOO⁻ being the major product in the potential range of -0.6 to -1.1 V vs. RHE (Fig. S12). The highest FE for HCOO⁻ was 73% at -0.9 V vs. RHE. Throughout the entire potential range, the FE for CO and H₂ remains lower than 22% and 19%, respectively. Unlike Ag/C and

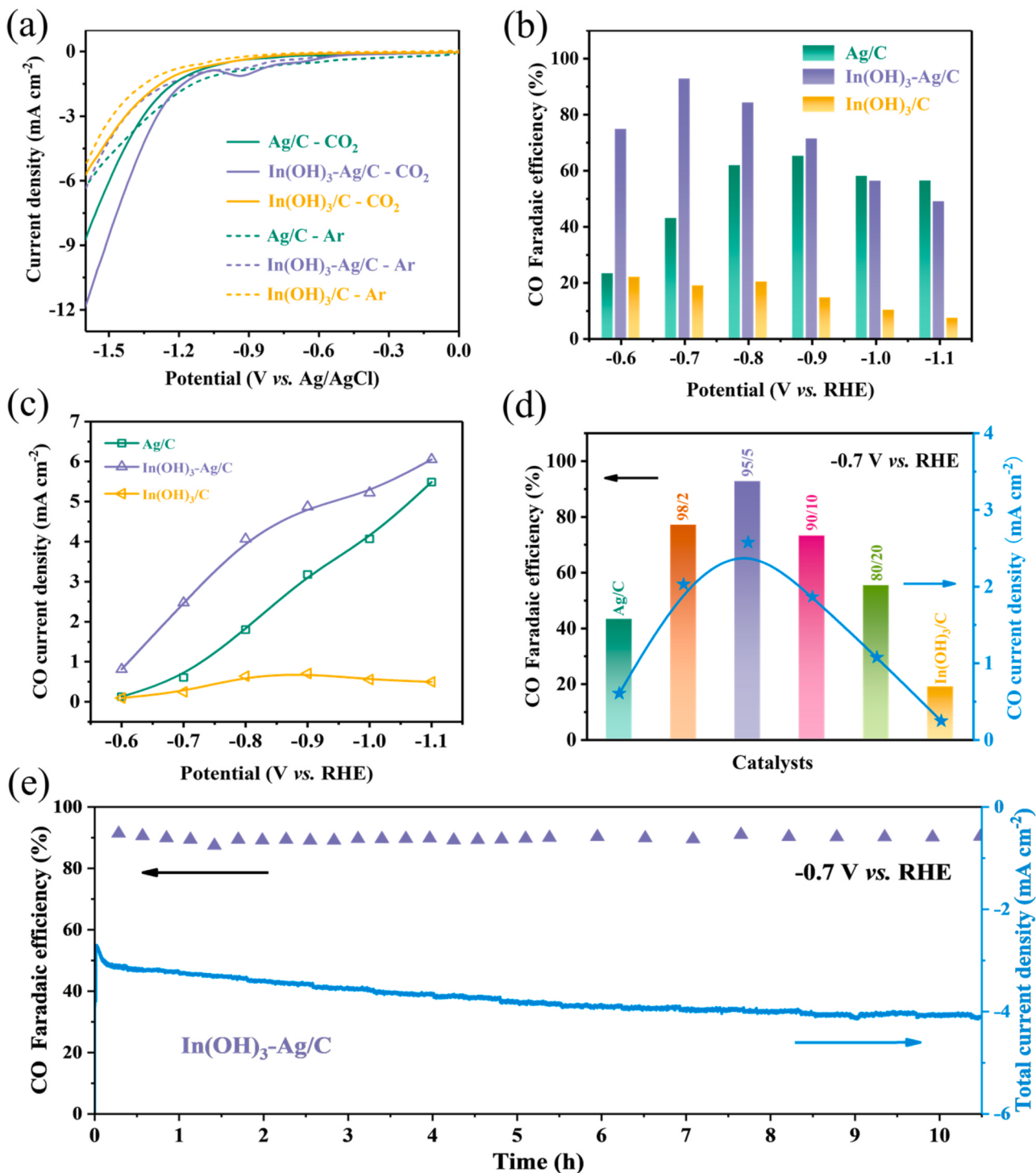


Fig. 3. (a) Comparison of LSV curves for Ag /C, In(OH)₃-Ag/C and In(OH)₃/C in CO₂-saturated 0.1 M KHCO₃ electrolyte at a scan rate of 10 mV s⁻¹. (b) Potential-dependent FEs and (c) partial current densities of CO at different potentials measured in CO₂-saturated 0.1 M KHCO₃ electrolyte. (d) Variation of FEs and CO partial current densities with various Ag/In feeding ratios on the catalysts at -0.7 V vs. RHE. (e) Stability performance of In(OH)₃-Ag/C catalyst at -0.7 V vs. RHE for over 10 h.

In(OH)₃/C, In(OH)₃-Ag/C catalyst can catalyze CO₂ electroreduction with higher FE for CO formation in the more positive potential range (Fig. S13). It was worth noting that within the entire working potential range from -0.6 to -1.1 V vs. RHE, In(OH)₃-Ag/C catalyst had the highest FE of 93% for CO production at -0.7 V vs. RHE (Fig. 3b). In addition, In(OH)₃-Ag/C catalyst also exhibited the highest CO current density, according to the results of the partial current densities of CO at various potentials measured on different catalysts (Fig. 3c). Compared

to other similar metal electrodes used to produce CO (Table S2), In(OH)₃-Ag/C catalyst showed an ideal FE and low overpotential.

To further evaluate the effect of In(OH)₃, the potential-dependent FEs of In(OH)₃-Ag/C (e.g., 98/2, 90/10, and 80/20) with different Ag/In feeding ratios were recorded (Fig. S14-S16). As depicted, all as-prepared catalysts gave the higher FE for CO as the major product compared with Ag catalyst. Typically, the highest FE for CO formation could reach 77% (-0.7 V vs. RHE) over Ag/In = 98/2. While with the

higher In(OH)_3 amount (90/10 and 80/20), the highest FE for CO reached to 84% (-0.8 V vs. RHE) and 59% (-0.6 V vs. RHE), respectively. Importantly, the FE for CO and current density on the catalysts at -0.7 V vs. RHE showed a clear volcano-shaped dependence on Ag/In feeding ratios (Fig. 3d). And this trend had been well confirmed in the whole applied potential (Fig. S17). The formate FE showed a different trend, which seem to be increased with the In(OH)_3 amount (Fig. S18). While H_2 FE showed a decrease trend with the increasing of In(OH)_3 amount. The lowest H_2 FE reached to about 5% on Ag/In = 80/20 at -0.9 V vs. RHE (Fig. S19). However, it should be noted that CO FE only reached about 45% when H_2 has the lowest FE. In addition, In_2O_3 -Ag/C was also used as a comparison sample (Fig. S20). The FEs for CO and CO partial current density of In_2O_3 -Ag/C (Fig. S21) were obviously lower than that of In(OH)_3 -Ag/C in the entire potential range, which was also consistent with the reports of Javier P rez-Ramirez et al. [39]. All these results suggested that the surface modification of Ag with In(OH)_3 and the formation of the interface could greatly influence the CO_2RR performance for maximizing the FE of CO.

Besides activity, the durability was another key to evaluate the CO_2RR performance. By measuring the current density and FE for CO at -0.7 V vs. RHE in long-term operation, the stability of In(OH)_3 -Ag/C

catalyst before and after electrolysis was investigated (Fig. 3e). Despite some fluctuations in the total current density, In(OH)_3 -Ag/C catalyst still held the high FE of near 90% over 10 h to produce CO. The small fluctuation of total current density may be due to the changes in electrolyte concentration and high local pH near the electrode surface [42, 43]. To further confirm the variation of catalyst before and after the reaction, the post-catalysis electrodes were rinsed with deionized water and dried at 40 °C in vacuum for further analysis, and the pre-catalysis reaction electrodes were used for comparison. The morphology of the In(OH)_3 -Ag/C remained stable after CO_2RR and no isolated In species were separated from Ag nanoparticles (Fig. S22). Furthermore, it was found that the phase of In(OH)_3 -Ag/C catalyst was well retained and no formation of specific alloys or intermetallic compounds (Fig. S23), demonstrating its structural stability. XPS measurements also presented that Ag and In still maintained the original state of metallic Ag^0 metal and In^{3+} ion (Fig. S24), verifying the stability of the element chemical state [16, 36].

3.3. Enhancement mechanism of CO_2RR activity

To verify whether the modification of In(OH)_3 on Ag nanoparticles

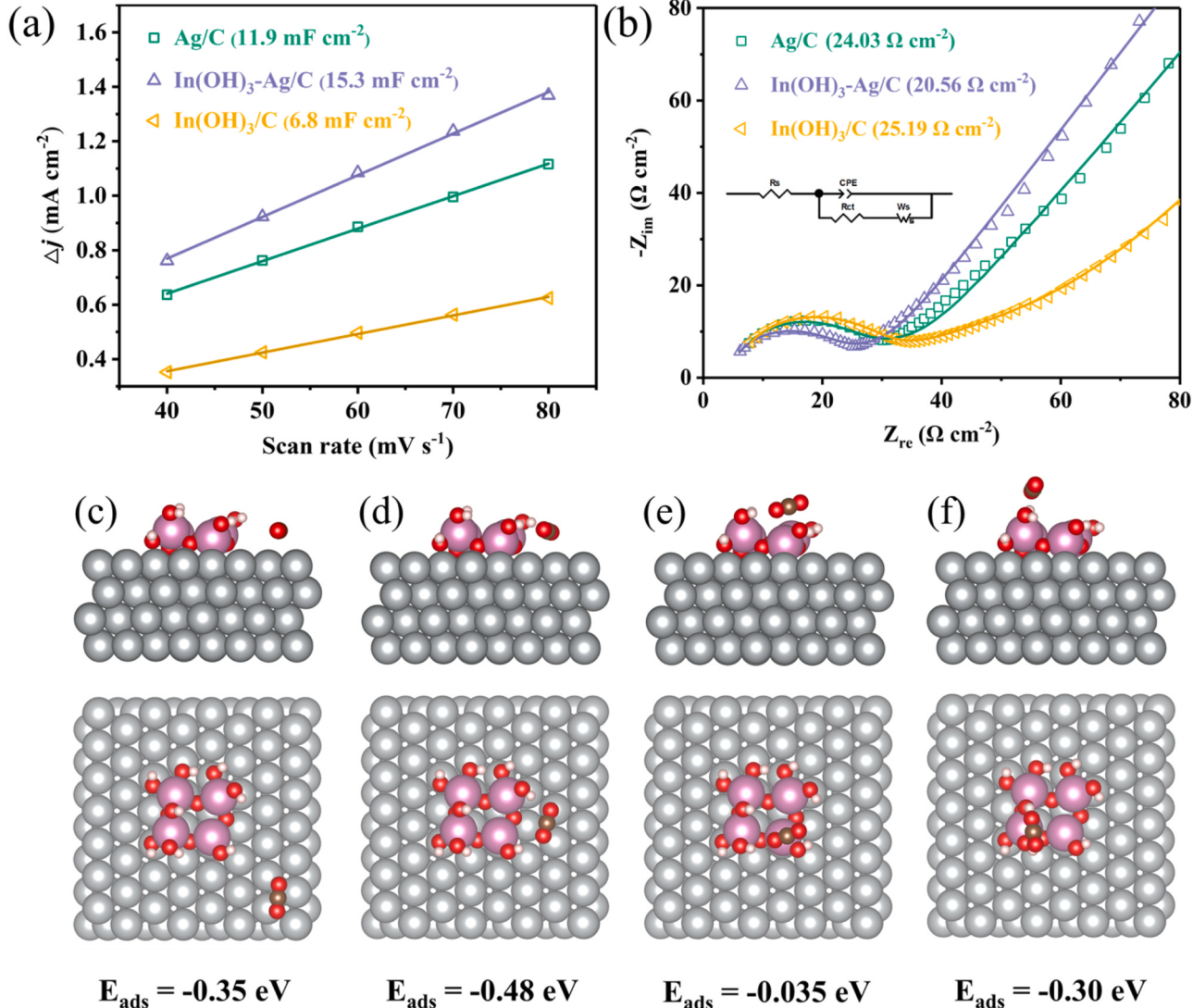


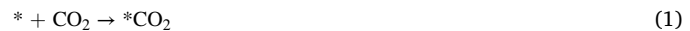
Fig. 4. (a) Charging current density differences plotted against scan rates. (b) Nyquist plots (the inset gives an equivalent circuit model used for the EIS simulations). Adsorption energy and adsorption configurations of CO_2 on (c) $\text{Ag}(111)$ slab, (d) $\text{In(OH)}_3\text{/Ag}(111)$ interface, (e) unsaturated In atom of In(OH)_3 cluster and (f) hydroxide of In(OH)_3 cluster. Grey balls are Ag, purple balls are In, red balls are O, brown balls are C, and white balls are H.

created new active sites for CO₂RR, according to the cyclic voltammetry (CV) measurements (Fig. S25), the electrochemical active surface area (ECSA) was compared by the double-layer capacitance (C_{dl}) in CO₂-saturated 0.1 M KHCO₃ electrolyte (Fig. 4a). The C_{dl} of In(OH)₃-Ag/C (up to 15.3 mF cm⁻²) was obviously higher than that of Ag/C (11.9 mF cm⁻²) and In(OH)₃/C (6.8 mF cm⁻²), clearly confirming that the In(OH)₃-Ag interface helped to expose more accessible active sites on the surface and improve the CO₂RR activity of In(OH)₃-Ag/C catalyst. And the C_{dl} for In(OH)₃-Ag/C catalyst with various Ag/In feeding ratios (e.g., 98/2, 90/10, and 80/20) were also higher than Ag/C and In(OH)₃/C, which was in line with that of all catalytic performances for CO FEs (Fig. S26). Importantly, compared to Ag/C catalyst, the specific current density of CO (normalized against ECSA) was also improved after In(OH)₃ decoration, except for Ag/In = 80/20 (Fig. S27). The larger specific current density of CO indicated that the intrinsic activity of the catalysts was the main factor for the CO₂RR performance [44,45]. Considering the fact as previously mentioned that the selectivity of CO decreased and formic acid selectivity seem to be increased with more In(OH)₃ amount, it was hypothesized that the decrease in specific current density of Ag/In = 80/20 was due to the effect of the competitive sites for formic acid generation produced by excessive In(OH)₃.

The kinetic improvement for CO₂RR caused by the In(OH)₃-Ag interface sites was further investigated by electrochemical impedance spectroscopy (EIS). As indicated in the Nyquist plots (Fig. 4b), the charge transfer resistance (R_{ct}) of In(OH)₃-Ag/C catalyst was smaller than other ones in the high frequency region, confirming that CO₂ molecules have a smaller interfacial charge-transfer resistance on In

(OH)₃-Ag/C catalyst. Similarly, other In(OH)₃-Ag/C catalysts with different In(OH)₃ amount also showed a lower R_{ct} compared to Ag/C and In(OH)₃/C catalysts (Fig. S28). These results implied that the interactions between Ag and In(OH)₃ could greatly enhance the electroconductivity and accelerate the charge transfer from catalyst surface to the adsorbed reaction intermediates, suggesting a faster kinetics for CO₂RR [46].

The combination of Ag and In(OH)₃ created a dramatic increase in the CO formation, suggesting that the In(OH)₃-Ag interface should modulate the adsorption of CO₂ and reaction intermediate on the catalyst [47]. The adsorption of CO₂ on the electrode surface was usually considered as the first step of CO₂RR. It is generally believed that the action pathway of CO₂→CO follows five equations [48,49], where * referred as an active site.



Therefore, density functional theory (DFT) calculation was executed to study the CO₂ adsorption energies on different sites (Fig. 4c-f). As depicted, CO₂ was more liable to be adsorbed on the In(OH)₃-Ag interface sites (E_{ads} is -0.48 eV). This result suggested that the modification

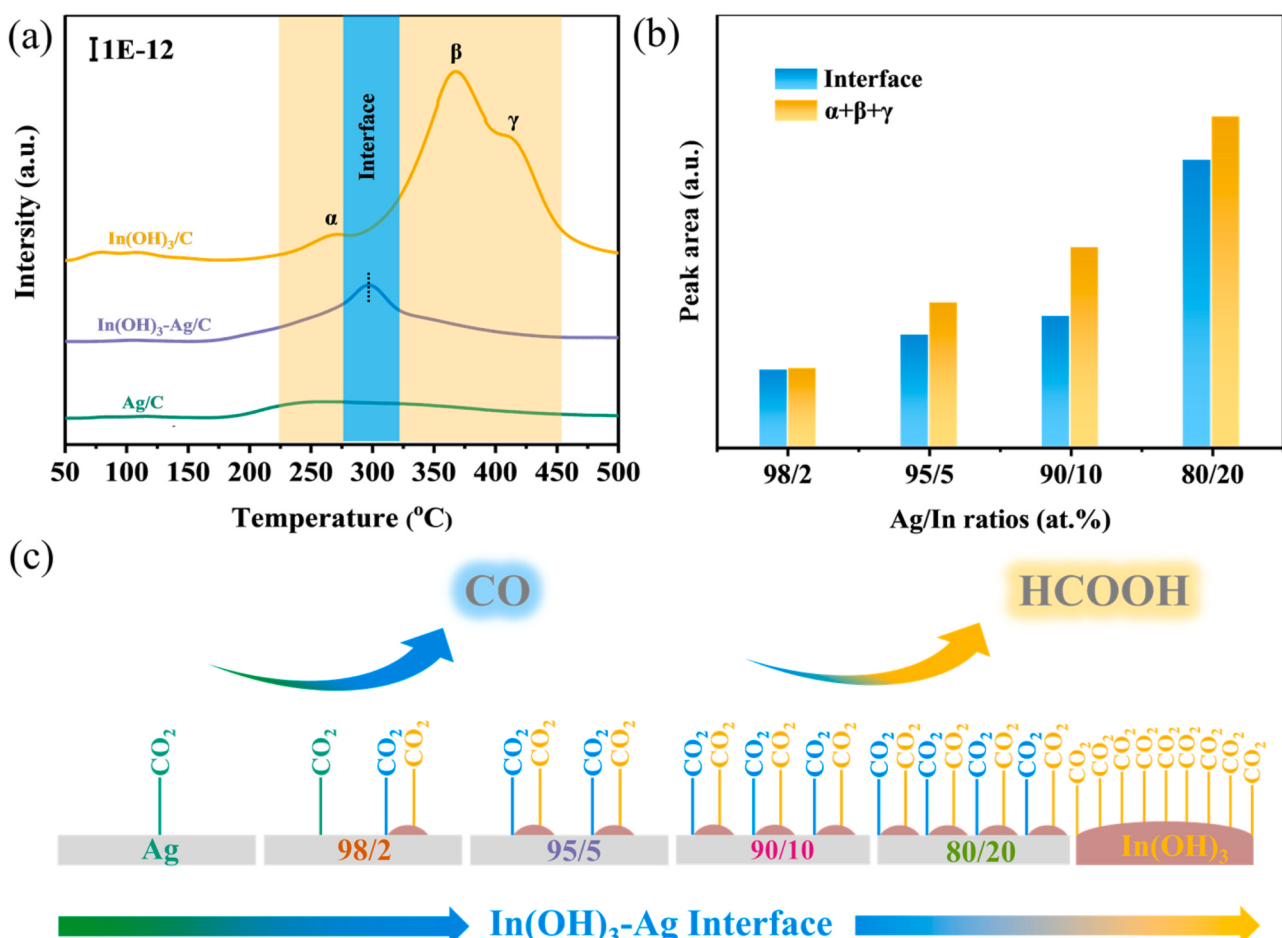


Fig. 5. (a) CO₂-TPD curves for Ag/C, In(OH)₃-Ag/C and In(OH)₃/C. (b) The amounts of relevant desorbed-CO₂ species (peak interface and peak $\alpha + \beta + \gamma$) over various Ag/In feeding ratios catalysts derived from the CO₂-TPD curves. (c) Diagram of CO₂ adsorption on different catalyst surfaces (Green, blue and yellow represent CO₂ adsorbed on Ag, In(OH)₃-Ag interface and In(OH)₃, respectively).

of In(OH)_3 on Ag nanoparticles surface significantly affected the CO_2 adsorption and activation, and CO_2 was more readily adsorbed at the $\text{In(OH)}_3\text{-Ag}$ interface sites.

The adsorption of CO_2 on the $\text{In(OH)}_3\text{-Ag}$ interface sites was further validated by CO_2 temperature programmed desorption ($\text{CO}_2\text{-TPD}$) measurements (Fig. 5a). It was demonstrated that an additional desorption peak between 290 and 310 °C after the decoration of In(OH)_3 on Ag surface, which could be ascribed to the binding site for CO_2 adsorption at the $\text{In(OH)}_3\text{-Ag}$ interface [50]. Actually, this unique desorption peak had also been observed in other Ag/In feeding ratios catalysts (Fig. S29). Obviously, the adsorption capacity of CO_2 was significantly improved as compared to that of Ag catalyst after In(OH)_3 decoration, which was beneficial to CO_2RR [12].

Furthermore, these adsorbed CO_2 species (where interface, α , β , and γ represent CO_2 adsorbed at $\text{In(OH)}_3\text{-Ag}$ interface sites, the weak base sites, medium-strong base sites, and strong base sites of In(OH)_3 , respectively) could be quantified by peak deconvolution over various Ag/In feeding ratios catalysts (Fig. 5b). Apparently, the interface sites were significantly increased with the increase in In amount because a higher amount of In(OH)_3 decoration would create a larger interfacial

region [50]. Meanwhile, the adsorption of CO_2 at the basic site of In(OH)_3 also increased significantly with the higher amount of In(OH)_3 decoration, and large amount of CO_2 adsorbed on the surface of In(OH)_3 tends to favor the formation of formate [51].

Based on the above discussion, a regulatory mechanism for product selectivity by CO_2 competitive adsorption between In(OH)_3 and $\text{In(OH)}_3\text{-Ag}$ interface sites was proposed (Fig. 5c). That was to say, although the high amount of In(OH)_3 decoration may produce more interfacial sites and CO_2 was more liable to be adsorbed on the $\text{In(OH)}_3\text{-Ag}$ interface sites, the basic sites of In(OH)_3 will strongly lead to the conversion of CO_2 to formate rather than CO, which was also in agree with our previous suggestion about the reason for the decrease in specific current density of Ag/In = 80/20.

Electrochemical *in situ* Raman spectroscopy can effectively monitor the changes of intermediate state products and catalyst surface structure. In order to get a fundamental understanding of the $\text{In(OH)}_3\text{-Ag}$ interface for CO_2RR enhancement mechanism, through the H-type *in situ* Raman electrolysis cell with optical window (Fig. S30), the changes of surface intermediates and surface structure for Ag/C (Fig. 6a) and $\text{In(OH)}_3\text{-Ag/C}$ (Fig. 6b) at different potentials (−0.3 to −1.1 V vs. RHE)

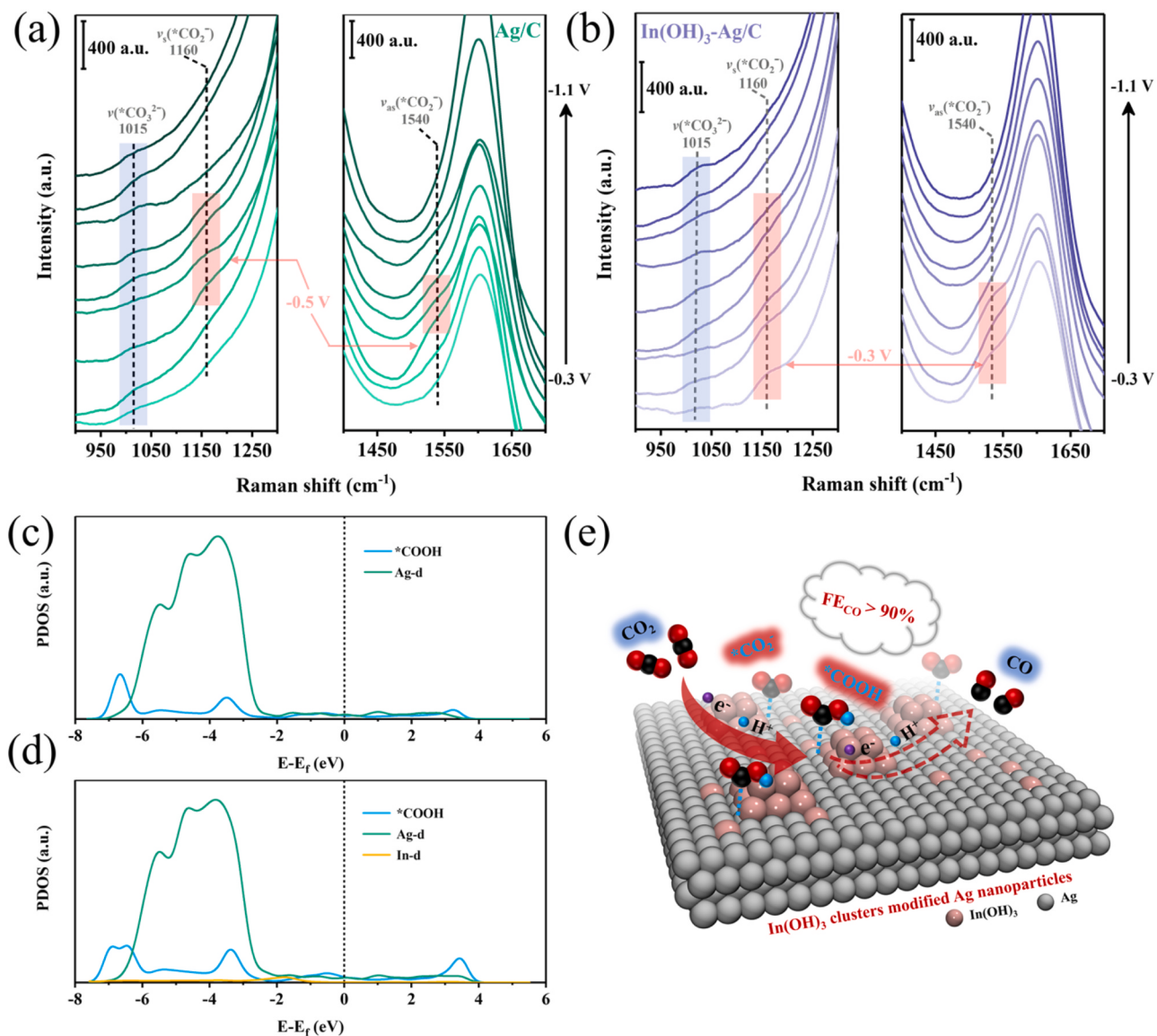


Fig. 6. Potential-dependent *in situ* Raman spectra of (a) Ag/C and (b) $\text{In(OH)}_3\text{-Ag/C}$ in CO_2 -saturated 0.1 M KHCO_3 electrolyte. PDOS of ${}^*\text{COOH}$ species adsorbed on (c) Ag(111) slab and (d) $\text{In(OH)}_3\text{/Ag(111)}$ interface. (e) Reaction route for boosting CO_2RR to CO over the $\text{In(OH)}_3\text{-Ag}$ interface sites.

were recorded using Renishaw confocal laser Raman spectrometer. As depicted, the peaks at 1015 cm^{-1} were almost constant with the potential because it originated from the CO_2^- adsorbed on the electrode surface in the electrolyte [52]. Meanwhile, the peaks located at 1160 cm^{-1} and 1540 cm^{-1} can be assigned to the symmetric stretching vibration of $^*\text{CO}_2^-$ ($\nu_s\text{ CO}_2^-$) and the asymmetric stretching vibration of $^*\text{CO}_2^-$ ($\nu_{as}\text{ CO}_2^-$), respectively [52–54]. It was well known that the initial electron transfer process associated with $^*\text{CO}_2^-$ was regarded as the rate-determining step for CO_2RR . And $^*\text{CO}_2^-$ strongly affect the formation of $^*\text{COOH}$, which was the key intermediate for the CO product during CO_2RR [11,52–54]. Obviously, $^*\text{CO}_2^-$ appeared on $\text{In(OH)}_3\text{-Ag/C}$ catalyst immediately when a negative -0.3 V vs. RHE was applied. However, for Ag/C catalyst, no significant $^*\text{CO}_2^-$ appeared until the negative potential increased to -0.5 V vs. RHE. This indicated that Ag/C and $\text{In(OH)}_3\text{-Ag/C}$ catalysts may undergo different CO_2 reduction mechanisms, in which $\text{In(OH)}_3\text{-Ag/C}$ catalyst probably exhibit a fast 1 e^- pre-equilibrium transfer to form $^*\text{CO}_2^-$ prior to a chemical H^+ transfer step, while Ag/C catalyst proceeded an initial rate-limiting 1 e^- transfer from CO_2 to $^*\text{CO}_2^-$ that needed a higher overpotentials. This result can be attributed to the acceleration of the interfacial charge transfer process (Fig. 4b). Subsequently, the characteristic peaks associated with $^*\text{CO}_2^-$ eventually disappeared as the potential became more negative for both Ag/C and $\text{In(OH)}_3\text{-Ag/C}$ catalysts [55,56]. This variation of characteristic peak intensity with potential may depend on the trade-off between adsorption and transformation of intermediate products [54]. As a result, $\text{In(OH)}_3\text{-Ag}$ interface can promote the generation of key $^*\text{CO}_2^-$ intermediate at a lower potential and thus facilitate CO_2RR .

The adsorption stability of $^*\text{COOH}$ on catalyst was found as another key factor for CO production. According to the metal-ligand bonding theory of organic-metal catalysis [57], the interactions between the catalyst and adsorption molecules mainly emanate from the σ -bonding and π -back bonding. Therefore, we calculated the partial density of states (PDOS) of $\text{Ag}(111)$ and $\text{In(OH)}_3/\text{Ag}(111)$ with $^*\text{COOH}$ species to analyze the different adsorptive action of $^*\text{COOH}$ on them (Fig. 6c, d). The calculated PDOS results showed that there existed much stronger hybridization between the 4d orbital from Ag and In atoms of $\text{In(OH)}_3/\text{Ag}(111)$ and 2p orbital from $^*\text{COOH}$, as compared to that for $\text{Ag}(111)$, leading to the stronger binding of the $^*\text{COOH}$ intermediate and the significantly enhancement of CO_2RR activity for $\text{In(OH)}_3\text{-Ag/C}$ catalyst [58]. Moreover, the $\text{In(OH)}_3/\text{Ag}(111)$ charge density difference showed that the interface formation resulted in the reduction of In^{3+} site (Fig. 2c, d). That also meant the key $^*\text{COOH}$ intermediate could be stabilized via the direct interaction between one of terminal oxygen and reduced In^{3+} site at the interface [12]. The stabilization of COOH over the catalyst surface was beneficial to lowering of CO_2RR overpotentials and enhancing the formation of adsorbed $^*\text{CO}$ species [59]. Thus, $\text{In(OH)}_3\text{-Ag/C}$ catalyst showed a higher FE_{CO} than Ag/C catalyst at lower overpotentials.

It has been well known from above studies that the In(OH)_3 fraction and the $\text{In(OH)}_3\text{-Ag}$ interface played a critical role in tuning the product distribution of CO_2RR . The enhanced CO_2RR performance of $\text{In(OH)}_3\text{-Ag/C}$ catalyst could be attributed to the establishment of $\text{In(OH)}_3\text{-Ag}$ interface (Fig. 6e). Appropriate In(OH)_3 clusters on Ag nanoparticles could effectively generate new highly active $\text{In(OH)}_3\text{-Ag}$ interface sites, and CO_2 was preferentially adsorbed at these interface sites. The $\text{In(OH)}_3\text{-Ag}$ interface accelerated the transfer of electrons to adsorbed CO_2 and promoted the formation of key $^*\text{CO}_2^-$ intermediate. In addition, $\text{In(OH)}_3\text{-Ag/C}$ catalyst can effectively strengthen the adsorption stability of $^*\text{COOH}$ intermediate by the formation of the $\text{In(OH)}_3\text{-Ag}$ interface in comparison with Ag/C catalyst. Indeed, the interface sites optimized the intrinsic active through electronic structure regulation, changed the adsorption and reaction characteristics of reactant molecules and intermediates, and thus enhanced CO_2RR activity.

4. Conclusions

In summary, it was demonstrated that the construction of $\text{In(OH)}_3\text{-Ag}$ interface significantly enhanced the activity and selectivity of CO_2RR . Compared to Ag/C and $\text{In(OH)}_3/\text{C}$, $\text{In(OH)}_3\text{-Ag/C}$ displayed the excellent catalytic selectivity in the electrochemical reduction of CO_2 into CO , realizing the FE_{CO} of 93% at -0.7 V vs. RHE. The high selectivity toward CO was attributed to the introduction of heterogeneous $\text{In(OH)}_3\text{-Ag}$ interface. Experimental and theoretical findings indicated that $\text{In(OH)}_3\text{-Ag}$ interface caused the larger electrochemical active area, faster electron transfer, and higher CO_2 adsorption ability. More importantly, the formation of $\text{In(OH)}_3\text{-Ag}$ interface was significantly favorable for the generation of key $^*\text{CO}_2^-$ intermediate at lower potential and strengthened the adsorption stability of $^*\text{COOH}$ intermediate. This work provided a novel idea for the rational design of high efficiency catalysts towards CO_2 electrochemical reduction by interfacial control.

CRediT authorship contribution statement

Liang Fu: Conceptualization; Data curation; Formal analysis; Investigation; Methodology; Software; Validation; Visualization; Writing - original draft. **Lingling Zhou:** Investigation; Software; Visualization. **Yue Ding:** Theoretical calculations, Methodology. **Zhenping Qu:** Funding acquisition; Project administration; Resources; Supervision; Validation; Writing - review & editing.

Declaration of Competing Interest

The authors declare that they have no known competing financial interests or personal relationships that could have appeared to influence the work reported in this paper.

Data availability

Data will be made available on request.

Acknowledgments

This work was financially supported by the National Natural Science Foundation of China (No. 22276022) and National Key Research and Development Program of China (No. 2019YFC1903903). HR-TEM, XRD and XPS data were obtained using equipment maintained by Instrumental Analysis Center, Dalian University of Technology. The authors acknowledge the assistance of DUT Instrumental Analysis Center.

Appendix A. Supporting information

Supplementary data associated with this article can be found in the online version at [doi:10.1016/j.apcatb.2023.123170](https://doi.org/10.1016/j.apcatb.2023.123170).

References

- [1] P. De Luna, C. Hahn, D. Higgins, S.A. Jaffer, T.F. Jaramillo, E.H. Sargent, What would it take for renewably powered electrosynthesis to displace petrochemical processes? *Science* 364 (2019).
- [2] F. Franco, C. Rettenmaier, H.S. Jeon, B. Roldan Cuenya, Transition metal-based catalysts for the electrochemical CO_2 reduction: from atoms and molecules to nanostructured materials, *Chem. Soc. Rev.* 49 (2020) 6884–6946.
- [3] M.B. Ross, P. De Luna, Y. Li, C.-T. Dinh, D. Kim, P. Yang, E.H. Sargent, Designing materials for electrochemical carbon dioxide recycling, *Nat. Catal.* 2 (2019) 648–658.
- [4] Y. Ye, H. Yang, J. Qian, H. Su, K.J. Lee, T. Cheng, H. Xiao, J. Yano, W. A. Goddard 3rd, E.J. Crumlin, Dramatic differences in carbon dioxide adsorption and initial steps of reduction between silver and copper, *Nat. Commun.* 10 (2019) 1875.
- [5] Y. Dong, Q. Zhang, Z. Tian, B. Li, W. Yan, S. Wang, K. Jiang, J. Su, C.W. Oloman, E. L. Gyenge, R. Ge, Z. Lu, X. Ji, L. Chen, Ammonia thermal treatment toward topological defects in porous carbon for enhanced carbon dioxide electroreduction, *Adv. Mater.* 32 (2020), e2001300.

[6] D. Gao, T. Liu, G. Wang, X. Bao, Structure sensitivity in single-atom catalysis toward CO_2 electroreduction, *ACS Energy Lett.* 6 (2021) 713–727.

[7] N.W. Kinzel, C. Werle, W. Leitner, Transition metal complexes as catalysts for the electroconversion of CO_2 : an organometallic perspective, *Angew. Chem. Int. Ed. Engl.* 60 (2021) 11628–11686.

[8] C.F. Wen, M. Zhou, P.F. Liu, Y. Liu, X. Wu, F. Mao, S. Dai, B. Xu, X.L. Wang, Z. Jiang, P. Hu, S. Yang, H.F. Wang, H.G. Yang, Highly ethylene-selective electrocatalytic CO_2 reduction enabled by isolated Cu-S motifs in metal-organic framework based precatalysts, *Angew. Chem. Int. Ed. Engl.* 61 (2022), e202111700.

[9] H. Li, T. Liu, P. Wei, L. Lin, D. Gao, G. Wang, X. Bao, High-rate CO_2 electroreduction to C_{2+} products over a copper-copper iodide catalyst, *Angew. Chem. Int. Ed. Engl.* 60 (2021) 14329–14333.

[10] L. Lin, T. Liu, J. Xiao, H. Li, P. Wei, D. Gao, B. Nan, R. Si, G. Wang, X. Bao, Enhancing CO_2 eLectroreduction to Methane with A cobalt phthalocyanine and zinc-nitrogen-carbon tandem catalyst, *Angew. Chem. Int. Ed. Engl.* 59 (2020) 22408–22413.

[11] X.-C. Sun, K. Yuan, J.-H. Zhou, C.-Y. Yuan, H.-C. Liu, Y.-W. Zhang, Au^{3+} species-induced interfacial activation enhances metal-support interactions for boosting electrocatalytic CO_2 reduction to CO, *ACS Catal.* 12 (2021) 923–934.

[12] D. Gao, Y. Zhang, Z. Zhou, F. Cai, X. Zhao, W. Huang, Y. Li, J. Zhu, P. Liu, F. Yang, G. Wang, X. Bao, Enhancing CO_2 electroreduction with the metal-oxide interface, *J. Am. Chem. Soc.* 139 (2017) 5652–5655.

[13] M. Luo, Z. Wang, Y.C. Li, J. Li, F. Li, Y. Lum, D.H. Nam, B. Chen, J. Wicks, A. Xu, T. Zhuang, W.R. Leow, X. Wang, C.T. Dinh, Y. Wang, Y. Wang, D. Sinton, E. H. Sargent, Hydroxide promotes carbon dioxide electroreduction to ethanol on copper via tuning of adsorbed hydrogen, *Nat. Commun.* 10 (2019) 5814.

[14] G.O. Larrazábal, A.J. Martín, S. Mitchell, R. Hauert, J. Pérez-Ramírez, Synergistic effects in silver-indium electrocatalysts for carbon dioxide reduction, *J. Catal.* 343 (2016) 266–277.

[15] W. Deng, L. Zhang, L. Li, S. Chen, C. Hu, Z.J. Zhao, T. Wang, J. Gong, Crucial role of surface hydroxyls on the activity and stability in electrochemical CO_2 reduction, *J. Am. Chem. Soc.* 141 (2019) 2911–2915.

[16] W. Yang, S. Chen, W. Ren, Y. Zhao, X. Chen, C. Jia, J. Liu, C. Zhao, Nanostructured amalgams with tuneable silver–mercury bonding sites for selective electroreduction of carbon dioxide into formate and carbon monoxide, *J. Mater. Chem. A* 7 (2019) 15907–15912.

[17] T.D. Kuhne, M. Iannuzzi, M. Del Ben, V.V. Rybkin, P. Seewald, F. Stein, T. Laino, R. Z. Khalilullin, O. Schutt, F. Schiffrmann, D. Golze, J. Wilhelm, S. Chulkov, M. H. Bani-Hashemian, V. Weber, U. Borstnik, M. Taillefumier, A.S. Jakobovits, A. Lazzaro, H. Pabst, T. Müller, R. Schade, M. Guidon, S. Andermatt, N. Holmberg, G.K. Schenter, A. Hehn, A. Bussy, F. Belleflamme, G. Tabacchi, A. Gloss, M. Lass, I. Bethune, C.J. Mundy, C. Plessl, M. Watkins, J. VandeVondele, M. Krack, J. Hutter, CP2K: An electronic structure and molecular dynamics software package - Quickstep: Efficient and accurate electronic structure calculations, *J. Chem. Phys.* 152 (2020), 194103.

[18] K.B. John, P. Perdew, Matthias Ernzerhof, Generalized gradient approximation made simple, *Phys. Rev. Lett.* 77 (1996) 3865–3868.

[19] J. VandeVondele, J. Hutter, Gaussian basis sets for accurate calculations on molecular systems in gas and condensed phases, *J. Chem. Phys.* 127 (2007), 114105.

[20] M.T.S. Goedecker, J. Hutter, Separable dual-space Gaussian pseudopotentials, *Phys. Rev. B* 54 (1996) 1703–1710.

[21] B.G. Lippert, J.H. Parrinello, Michele, A hybrid Gaussian and plane wave density functional scheme, *Mol. Phys.* 92 (2010) 477–488.

[22] T. Lu, F. Chen, Multiwfn: a multifunctional wavefunction analyzer, *J. Comput. Chem.* 33 (2012) 580–592.

[23] K. Momma, F. Izumi, VESTA3 for three-dimensional visualization of crystal, volumetric and morphology data, *J. Appl. Crystallogr.* 44 (2011) 1272–1276.

[24] G.J. Martyna, M.E. Tuckerman, A reciprocal space based method for treating long range interactions in ab initio and force-field-based calculations in clusters, *J. Chem. Phys.* 110 (1999) 2810–2821.

[25] N. Li, W. Wang, L. Song, H. Wang, Q. Fu, Z. Qu, CO_2 hydrogenation to methanol promoted by Cu and metastable tetragonal $\text{Ce}_x\text{Zr}_y\text{O}_z$ interface, *J. Energy Chem.* 68 (2022) 771–779.

[26] Q. Zhao, H. Li, Y. Cao, Effect of $\text{In}(\text{OH})_3$ species modified ZnS on improved photocatalytic activity of photoreduction of CO_2 , *J. Solid State Chem.* 296 (2021).

[27] Y. Zhou, R. Zhou, X. Zhu, N. Han, B. Song, T. Liu, G. Hu, Y. Li, J. Lu, Y. Li, Mesoporous PdAg nanospheres for stable electrochemical CO_2 reduction to formate, *Adv. Mater.* 32 (2020), e2000992.

[28] D. Pavesi, F. Dattila, R.C.J. Van de Poll, D. Anastasiadou, R. García-Muelas, M. Figueiredo, G.-J.M. Gruter, N. López, M.T.M. Koper, K.J.P. Schouten, Modulation of the selectivity of CO_2 to CO electroreduction in palladium rich Palladium-Indium nanoparticles, *J. Catal.* 402 (2021) 229–237.

[29] D. Pavesi, F.S.M. Ali, D. Anastasiadou, T. Kallio, M. Figueiredo, G.-J.M. Gruter, M. T.M. Koper, K.J.P. Schouten, CO_2 electroreduction on bimetallic Pd-In nanoparticles, *Catal. Sci. Technol.* 10 (2020) 4264–4270.

[30] D.C. Cuiqing Wang, * Xulind Jiao*, Changlong Chen, Lotus-root-like In_2O_3 nanostructures: fabrication, characterization, and photoluminescence properties, *J. Phys. Chem. C* 111 (2007) 13398–13403.

[31] Z. Qu, D. Chen, Y. Sun, Y. Wang, High catalytic activity for formaldehyde oxidation of $\text{Ag}/\text{Co}/\text{APTES}@\text{MCM-41}$ prepared by two steps method, *Appl. Catal. A: Gen.* 487 (2014) 100–109.

[32] Z. Cai, Y. Wu, Z. Wu, L. Yin, Z. Weng, Y. Zhong, W. Xu, X. Sun, H. Wang, Unlocking bifunctional electrocatalytic activity for CO_2 reduction reaction by win-win metal-oxide cooperation, *ACS Energy Lett.* 3 (2018) 2816–2822.

[33] J. Li, A. Ozden, M. Wan, Y. Hu, F. Li, Y. Wang, R.R. Zamani, D. Ren, Z. Wang, Y. Xu, D.-H. Nam, J. Wicks, B. Chen, X. Wang, M. Luo, M. Graetzel, F. Che, E.H. Sargent, D. Sinton, Silica-copper catalyst interfaces enable carbon-carbon coupling towards ethylene electrosynthesis, *Nat. Commun.* 12 (2021).

[34] R. Li, X. Xu, B. Zhu, X.Y. Li, Y. Ning, R. Mu, P. Du, M. Li, H. Wang, J. Liang, Y. Chen, Y. Gao, B. Yang, Q. Fu, X. Bao, In situ identification of the metallic state of Ag nanoclusters in oxidative dispersion, *Nat. Commun.* 12 (2021) 1406.

[35] W.H. Lee, Y.-J. Ko, Y. Choi, S.Y. Lee, C.H. Choi, Y.J. Hwang, B.K. Min, P. Strasser, H.-S. Oh, Highly selective and scalable CO_2 to CO - Electrolysis using coral-nanostructured Ag catalysts in zero-gap configuration, *Nano Energy* 76 (2020).

[36] Y. Liang, W. Zhou, Y. Shi, C. Liu, B. Zhang, Unveiling in situ evolved $\text{In}/\text{In}_2\text{O}_3-\text{x}$ heterostructure as the active phase of In_2O_3 toward efficient electroreduction of CO_2 to formate, *Sci. Bull.* 65 (2020) 1547–1554.

[37] Z. Sun, X. Wu, D. Guan, X. Chen, J. Dai, Y. Gu, S. She, W. Zhou, Z. Shao, One pot-synthesized Ag/Ag -doped CeO_2 nanocomposite with rich and stable 3D interfaces and Ce^{3+} for efficient carbon dioxide electroreduction, *ACS Appl. Mater. Interfaces* 13 (2021) 59993–60001.

[38] H. He, J. Wu, X. Yu, D. Xia, Y. Wang, F. Chen, L. Wang, L. Wu, J. Huang, N. Zhao, L. Deng, Y.-N. Liu, Dual-active sites design of $\text{Sn}_x\text{Sb}_y\text{-O}$ -GO nanosheets for enhancing electrochemical CO_2 reduction via Sb-accelerating water activation, *Appl. Catal. B: Environ.* 307 (2022).

[39] G.O. Larrazábal, A.J. Martín, S. Mitchell, R. Hauert, J. Pérez-Ramírez, Synergistic effects in silver–indium electrocatalysts for carbon dioxide reduction, *J. Catal.* 343 (2016) 266–277.

[40] F. Sastre, M.J. Muñoz-Batista, A. Kubacka, M. Fernández-García, W.A. Smith, F. Kapteijn, M. Makkee, J. Gascon, Efficient electrochemical production of syngas from CO_2 and H_2O by using a nanostructured $\text{Ag}/\text{g-C}_3\text{N}_4$ catalyst, *ChemElectroChem* 3 (2016) 1497–1502.

[41] X. Zhang, Z. Chen, M. Jiao, X. Ma, K. Mou, F. Cheng, Z. Wang, X. Zhang, L. Liu, Defects and conductive nitrogen-carbon framework regulated ZnInO_x nanosheets for boosting CO_2 electrocatalytic reduction, *Appl. Catal. B: Environ.* 279 (2020).

[42] Z. Chen, T. Fan, Y.-Q. Zhang, J. Xiao, M. Gao, N. Duan, J. Zhang, J. Li, Q. Liu, X. Yi, J.-L. Luo, Wavy SnO_2 catalyzed simultaneous reinforcement of carbon dioxide adsorption and activation towards electrochemical conversion of CO_2 to HCOOH , *Appl. Catal. B: Environ.* 261 (2020).

[43] T. Fan, W. Ma, M. Xie, H. Liu, J. Zhang, S. Yang, P. Huang, Y. Dong, Z. Chen, X. Yi, Achieving high current density for electrocatalytic reduction of CO_2 to formate on bismuth-based catalysts, *Cell Rep. Phys. Sci.* 2 (2021).

[44] P.-F. Sui, S. Liu, C. Xu, J. Xiao, N. Duan, R. Feng, J.-L. Luo, Directionally maximizing CO selectivity to near-unity over cupric oxide with indium species for electrochemical CO_2 reduction, *Chem. Eng. J.* 427 (2022).

[45] Z. Geng, X. Kong, W. Chen, H. Su, Y. Liu, F. Cai, G. Wang, J. Zeng, Oxygen vacancies in ZnO nanosheets enhance CO_2 electrochemical reduction to CO, *Angew. Chem. Int. Ed. Engl.* 57 (2018) 6054–6059.

[46] L. Peng, Y. Wang, I. Masood, B. Zhou, Y. Wang, J. Lin, J. Qiao, F.-Y. Zhang, Self-growing Cu/Sn bimetallic electrocatalysts on nitrogen-doped porous carbon cloth with 3D-hierarchical honeycomb structure for highly active carbon dioxide reduction, *Appl. Catal. B: Environ.* 264 (2020).

[47] D. Gao, R.M. Arán-Ais, H.S. Jeon, B. Roldan Cuena, Rational catalyst and electrolyte design for CO_2 electroreduction towards multicarbon products, *Nat. Catal.* 2 (2019) 198–210.

[48] B. Wei, Y. Xiong, Z. Zhang, J. Hao, L. Li, W. Shi, Efficient electrocatalytic reduction of CO_2 to HCOOH by bimetallic In-Cu nanoparticles with controlled growth facet, *Appl. Catal. B: Environ.* 283 (2021).

[49] W. Luo, J. Zhang, M. Li, A. Züttel, Boosting CO production in electrocatalytic CO_2 reduction on highly porous Zn catalysts, *ACS Catal.* 9 (2019) 3783–3791.

[50] J. Yin, Z. Gao, F. Wei, C. Liu, J. Gong, J. Li, W. Li, X. Xiao, G. Wang, J. Lu, L. Zhuang, Customizable CO_2 Electroreduction to C_1 or C_{2+} Products through Cu_y/CeO_2 Interface Engineering, *ACS Catal.* 12 (2022) 1004–1011.

[51] A. Rabiee, D. Nematollahi, Electrochemical reduction of CO_2 to formate ion using nanocubic mesoporous $\text{In}(\text{OH})_3$ /carbon black system, *Mater. Chem. Phys.* 193 (2017) 109–116.

[52] B. Zhang, Y. Chang, Y. Wu, Z. Fan, P. Zhai, C. Wang, J. Gao, L. Sun, J. Hou, Regulating $^{\bullet}\text{OCHO}$ intermediate as rate-determining step of defective oxynitride nanosheets enabling robust CO_2 electroreduction, *Adv. Energy Mater.* 12 (2022).

[53] W. Shan, R. Liu, H. Zhao, Z. He, Y. Lai, S. Li, G. He, J. Liu, In situ surface-enhanced raman spectroscopic evidence on the origin of selectivity in CO_2 electrocatalytic reduction, *ACS Nano* 14 (2020) 11363–11372.

[54] J. Duan, T. Liu, Y. Zhao, R. Yang, Y. Zhao, W. Wang, Y. Liu, H. Li, Y. Li, T. Zhai, Active and conductive layer stacked superlattices for highly selective CO_2 electroreduction, *Nat. Commun.* 13 (2022) 2039.

[55] S. Gao, X. Jiao, Z. Sun, W. Zhang, Y. Sun, C. Wang, Q. Hu, X. Zu, F. Yang, S. Yang, L. Liang, J. Wu, Y. Xie, Ultrathin Co_3O_4 layers realizing optimized CO_2 electroreduction to formate, *Angew. Chem. Int. Ed. Engl.* 55 (2016) 698–702.

[56] H. Dong, L. Zhang, L. Li, W. Deng, C. Hu, Z.J. Zhao, J. Gong, Abundant Ce^{3+} ions in Au/CeO_x nanosheets to enhance CO_2 electroreduction performance, *Small* 15 (2019), e1900289.

[57] Z. Wang, J. Zhao, Q. Cai, CO₂ electroreduction performance of a single transition metal atom supported on porphyrin-like graphene: a computational study, *Phys. Chem. Chem. Phys.* 19 (2017) 23113–23121.

[58] P. Lu, X. Tan, H. Zhao, Q. Xiang, K. Liu, X. Zhao, X. Yin, X. Li, X. Hai, S. Xi, A.T. S. Wee, S.J. Pennycook, X. Yu, M. Yuan, J. Wu, G. Zhang, S.C. Smith, Z. Yin, Atomically dispersed indium sites for selective CO₂ electroreduction to formic acid, *ACS Nano* 15 (2021) 5671–5678.

[59] D. Yang, Q. Zhu, X. Sun, C. Chen, W. Guo, G. Yang, B. Han, Electrosynthesis of a defective indium selenide with 3D structure on a substrate for tunable CO₂ electroreduction to syngas, *Angew. Chem. Int. Ed. Engl.* 59 (2020) 2354–2359.